We are IntechOpen,
the world's leading publisher of
Open Access books
Built by scientists, for scientists

6,900
Open access books available

185,000
International authors and editors

200M
Downloads

154
Countries delivered to

Our authors are among the

TOP 1%
most cited scientists

12.2%
Contributors from top 500 universities

CLARIVATE ANALYTICS
BOOK CITATION INDEX
INDEXED

WEB OF SCIENCE™

Selection of our books indexed in the Book Citation Index
in Web of Science™ Core Collection (BKCI)

Interested in publishing with us?
Contact book.department@intechopen.com

Numbers displayed above are based on latest data collected.
For more information visit www.intechopen.com

Effectiveness of a Helix Tube to Water Cool a Battery Module

Desmond Adair, Kairat Ismailov and
Zhumabay Bakenov

Additional information is available at the end of the chapter

Abstract

This chapter presents an investigation of the effectiveness of water cooling a battery module using a heat-sink prototype in the form of a thin copper helix tube within an aluminium block. A thermal model for the module containing six single cells is developed and numerically solved by coupling the heat energy transport equation with the fluid governing equations. The rate of generation of heat from the cells is calculated using a 2D model of a single cell with the resulting heat flux used as a Neumann boundary condition for the energy equation within a computational fluid dynamics code. Particular attention is given to the battery module operating in extreme ambient temperature conditions. The cooling strategy used is shown to satisfy two of the main concerns when managing the thermal performance of a battery module, that is, a suitable operating temperature range is maintained, and there is reasonable uniformity of temperature across the battery module. This should increase the battery cell life cycle together with enhancement of the charge and discharge performances. Variation of parameters such as the velocity of water within the tube and the number of turns used for the helix were investigated.

Keywords: Li-ion battery, convective heat transfer, clean energy

1. Introduction

Due to their outstanding properties regarding high energy density, power density, high service life, low self-discharge and rare pollution, the use of lithium ion batteries for battery electric vehicles (BEVs) and hybrid electric vehicles (HEVs) shows excellent promise [1]. Battery charging and discharging are strongly coupled to the operating temperature with a higher temperature increasing the number of undesired reactions, that is, the decomposition of the

electrolyte, thickening of the solid electrolyte interface (SEI) film, and so on, which have the effect of degrading the battery capacity [2–4]. Lithium-ion battery cells are also highly sensitive to low temperatures. For example, at below −10°C, it has been shown that batteries' performance deteriorates considerably [5, 6]. Safety is also an issue in that at high temperatures, lithium-ion batteries are prone to uncontrollable temperature build-up (thermal runaway) [7]. In addition, a battery pack is usually composed of up to hundreds of single cells connected in series and/or in parallel to produce output voltage and power/energy capacity to achieve the BEVs' or HEVs' operating needs. This contributes to the accumulation of heat and uneven temperature distributions across the battery pack so degrading performance. To counteract these serious problems, it is necessary to cool a battery pack effectively and uniformly.

Important to the development of a realistic thermal model of a battery module is good knowledge of heat generation either from the battery module as a whole or from individual cells within the module. The battery heat generation rate can be estimated by direct measurement [8], by indirect measurement, for example by measuring equilibrium voltage [9], measuring internal electrical resistance [10] or using the electrochemical mechanism [11, 12]. For direct measurement, the results apply to only a few operating points, and for indirect measurements, accuracy is a problem as the heat generation rate is a nonlinear function of the state of charge (SOC), current and operating temperature [13]. Work on single cell thermal-electrochemical modelling has already been done [13–16], and it is the view here that an essential component for the modelling of battery modules and eventually battery packs is to start with accurate calculations of heat generation within a given single cell.

There are a number of ways of cooling battery modules with the major division being between air cooling and liquid cooling. There are advantages and disadvantages associated with each choice. For liquid cooling systems, a disadvantage is that they have the potential to leak, which could cause an electrical short. Also when liquid is used, maintenance and repair can be more costly and more complicated, and generally liquid cooled systems are more heavy and require more components. However, a design can be used, as in the present application where the battery module and liquid can be separated by aluminium. Air cooling systems are generally less effective at maintaining a uniform temperature within and between cells in a battery module, and they cannot carry as much heat away from the battery as quickly as a liquid-based system. Air convection (natural or forced) quite often is insufficient for effective heat dissipation from batteries under abuse conditions leading often to nonuniform temperature distributions within battery packs [17, 18]. Although air cooling systems are lighter, have a lower cost and generally a longer life, water cooling is favoured for this work due to its much superior cooling effect. There are many investigations of cooling systems reported in the literature with the majority of the work focusing on lumped parameter models [19]. The effectiveness of passive air cooling using phase change materials (PCMs) combined with forced cooling has been investigated [17], as has different single cell spacing arrangements [11, 20, 21]. It has been stated and demonstrated in the literature that indirect liquid cooling of battery packs (both passive and active) can prove an efficient method for dissipation or addition of heat [22–25].

This chapter presents an investigation of the thermal performance of indirect water cooling, using the proposed design prototype of a thin copper helix tube contained within an aluminium

block, for a lithium ion battery module. A thermal model is developed for the battery module where electrochemical equations are solved to provide boundary conditions for a computational fluid dynamics code in which the energy and fluid flow conservation equations are solved. Variation of parameters such as the velocity of water within the tube and the number of turns used for the helix were investigated.

2. Mathematical model

2.1. Modelling within a single cell

The mathematical model for a single lithium-ion battery developed here is based on the work of Doyle et al. [26]. The battery cells used are cylindrical with a central mandrel, with thin layers of anode, cathode, current collector and separator rolling up on the mandrel and with protection provided by a battery can. The anode is made of graphite derivatives and the cathode material is a metallic oxide such as $LiFePO_4$ and LiM_2O_4. A schematic of a lithium ion cell is shown in **Figure 1**.

Generally, a lithium ion battery consists of the current collector, the positive electrode, the separator and the negative electrode. A lithiated organic solution fills the porous components and serves as the electrolyte. Several assumptions are needed, that is, the active electrode material is composed of spherical particles with uniform radius and the winding zone of the battery is a lumped model with homogeneous electrochemical properties. The material balance for the Li ions in an active solid material particle is governed by Fick's second law, here expressed in spherical coordinates
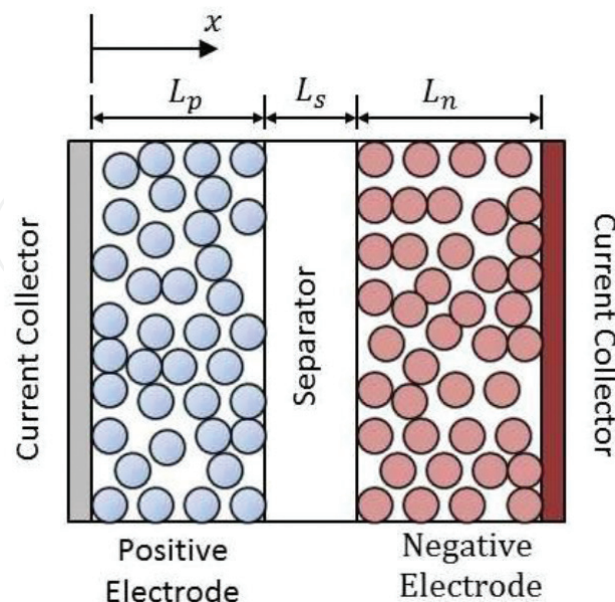

Figure 1. Schematic of a lithium ion battery.

$$\frac{\partial c_{s,i}}{\partial t} = D_{s,i} \frac{1}{r^2} \frac{\partial}{\partial r} \left(r^2 \frac{\partial c_{s,i}}{\partial r} \right), \tag{1}$$

where $i = p, s$ and $i = n$ for the positive and negative electrodes, respectively. At the centre of the particle, there is no flux, and on the surface of the particle, the flux is equal to the consuming/producing rate of Li ions due to the chemical reaction occurring at the solid/liquid surface giving the boundary conditions

$$-D_{s,i} \frac{\partial c_{s,i}}{\partial r} \bigg|_{r=0} = 0, \quad -D_{s,i} \frac{\partial c_{s,i}}{\partial r} \bigg|_{r=r_s} = J, \tag{2}$$

where J is the flux of lithium ions away from the surface of the spherical particles. The mass conservation of Li in the electrode solution is given by the concentration solution theory and can be expressed as

$$\varepsilon'_i \frac{\partial c_i}{\partial t} = D_{eff,i} \frac{\partial^2 c_i}{\partial x^2} + \left(1 - t^0_+\right) a_i J_i, \tag{3}$$

where $i = p, s$ and n and a_i are the electrode surface area per unit volume of the electrode. In the separator, the pore wall flux J_s is equal to zero, and at the two ends of the cell in the x-direction, there is no mass flux

$$-D_{eff,p} \frac{\partial c_p}{\partial x} \bigg|_{x=0} = 0, \quad -D_{eff,n} \frac{\partial c_n}{\partial x} \bigg|_{x=L_p+L_s+L_n} = 0 \tag{4}$$

At the interfaces between the positive electrode/separator and separator/negative electrode, the concentration of the binary electrolyte and its flux is continuous

$$c_p \big|_{x=L_p^-} = c_s \big|_{x=L_p^+}, \quad c_s \big|_{x=(L_p+L_s)^-} = c_n \big|_{x=(L_p+L_s)^+}, \tag{5}$$

$$-D_{eff,p} \frac{\partial c_p}{\partial x} \bigg|_{x=L_p^-} = -D_{eff,s} \frac{\partial c_s}{\partial x} \bigg|_{x=L_p^+} \tag{6}$$

$$-D_{eff,s} \frac{\partial c_s}{\partial x} \bigg|_{x=L_p^-} = -D_{eff,n} \frac{\partial c_n}{\partial x} \bigg|_{x=(L_p+L_s)^+} \tag{7}$$

The effective diffusion coefficient, D_{eff} of Li in the electrode can be represented as $D_{eff,i} = D_{\epsilon,i} \varepsilon_i^{brugg_i}$. The specific surface area for the electrode particles, a, is given by $a = 3\varepsilon_s/r_s$.

The charge balance in the solid phase is governed by Ohm's law

$$\sigma_{eff,i} \frac{\partial^2 \phi_{s,i}}{\partial x^2} = a_i F J_i \tag{8}$$

where $i = p$ and n. Here σ_{eff} is the effective electric conductivity and is given by $\sigma_{eff} = \sigma \cdot \varepsilon_s$.

The boundary conditions are expressed as

$$-\sigma_{eff,p}\frac{\partial\phi_{s,p}}{\partial x}\bigg|_{x=0} = I_{app}, \quad -\sigma_{eff,p}\frac{\partial\phi_{s,p}}{\partial x}\bigg|_{x=L_p} = 0, \quad -\sigma_{eff,n}\frac{\partial\phi_{s,n}}{\partial x}\bigg|_{x=L_p+L_s} = 0 \tag{9}$$

The potential of the solid phase at the right end of the cell (**Figure 1**) is set to zero, $\phi_{s,n}\big|_{x=L_p+L_s+L_n} = 0$ and the potential of the solid phase at $x = 0, \phi_{1,p}\big|_{x=0}$ is equal to E_{cell}. The charge balance in the liquid phase is based on Ohm's law, and it is given by

$$-\frac{\partial}{\partial x}\left(\kappa_{eff,i}\frac{\partial\phi_{2,i}}{\partial x}\right) + \frac{2RT(1-t^+)}{F_d}\frac{\partial}{\partial x}\left(\kappa_{eff,i}\frac{\partial(\ln c_i)}{\partial x}\right) = \frac{F_d}{F_i}J_i \tag{10}$$

where $i = p, s$ and n, and, the specific conductivity of the electrolyte is a function of the concentration of the electrolyte in the liquid phase [27]

$$\kappa_{eff,i} = \kappa_i\varepsilon_i^{brugg_i} \tag{11}$$

At the two ends of the cell, there is no charge flux in the liquid phase

$$-\kappa_{eff,p}\frac{\partial\phi_{2,p}}{\partial x}\bigg|_{x=0} = 0, \quad -\kappa_{eff,n}\frac{\partial\phi_{2,n}}{\partial x}\bigg|_{x=L_p+L_s+L_n} = 0 \tag{12}$$

In the abovementioned equations, the pore wall flux, J_i is determined by the Butler-Volmer equation

$$J_i = k_i\left(c_{s,i,maz} - c_s\big|_{r=r_s}\right)^{\alpha_a}\cdot c_s\big|_{r=r_s}^{\alpha_c}\cdot c^{\alpha_a}\left\{\exp\left(\frac{\alpha_a F\eta_i}{RT}\right) - \exp\left(-\frac{\alpha_c F\eta_i}{RT}\right)\right\} \tag{13}$$

where η_i is the over-potential of battery electrodes and is given by

$$\eta_i = \phi_{s,i} - \phi_{2,i} - U_i \tag{14}$$

The open circuit voltage of the electrode materials U_i is determined by cell temperature and Li concentrations at the surface of the spherical particle. The energy balance is given by [15]

$$\rho C_p\frac{\partial T}{\partial t} = \nabla\cdot\nabla(k_T T) + Q_{rea} + Q_{rev} + Q_{ohm} \tag{15}$$

with the boundary conditions determined by Newton's cooling law

$$-\lambda\frac{\partial T}{\partial x}\bigg|_{x=0} = h(T_\infty - T), \quad -\lambda\frac{\partial T}{\partial x}\bigg|_{x=L_p+L_s+L_n} = h(T - T_\infty) \tag{16}$$

where h is the heat transfer coefficient, T_∞ is the ambient temperature, $\dot{Q}_{rea}$ is the total reaction heat generation rate, $\dot{Q}_{rev}$ is the total reversible heat generation rate, $\dot{Q}_{ohm}$ is the total ohmic heat generation rate. The heat fluxes are defined by

$$\dot{Q}_{rea} = aFJ_i\eta_i \qquad (17)$$

$$\dot{Q}_{rev} = aFJ_iT \cdot \frac{dU_i}{dT} \qquad (18)$$

$$\dot{Q}_{ohm} = \sigma_{eff}\left(\frac{\partial\phi_s}{\partial x}\right)^2 + \kappa_{eff}\left(\frac{\partial\phi_2}{\partial x}\right)^2 + \frac{2k_{eff}RT\left(1 - t_+^0\right)}{F}\left(1 + \frac{d\ln f_\pm}{d\ln c}\right)\frac{\partial\ln c}{\partial x}\frac{\partial\phi_2}{\partial x} + aFJ_i\Delta\phi_{SEI} \qquad (19)$$

2.2. Modelling within the aluminium block

The battery module cooling system used here is a heat sink approach, where the lithium-ion battery cells are placed in an aluminium block and also surrounded by a copper helix coil through which water is pumped. The method employed is fundamentally to surround the cells with a conducting material, that is, a form of heat sink, and to remove or add heat using fluid. The cooling design is shown in **Figure 2**. The model solves in 3D, with fluid pumped through a central vertical tube and returned through the copper helix tube just within the aluminium block for efficient heat transfer and protection against damage.
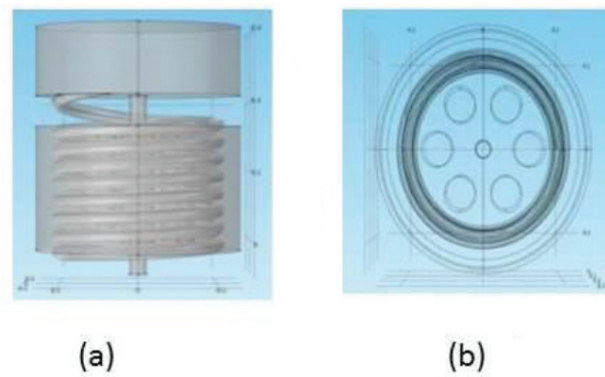

(a)   (b)

Figure 2. Copper helix coil within the aluminium block a. front and b. plan.
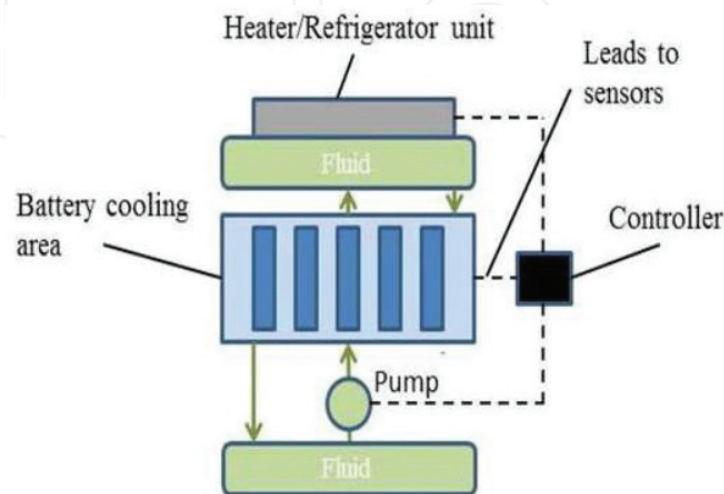

Figure 3. Schematic of thermal management system.

The fluid is conditioned using a heater/refrigerator unit placed on the top surface of the plenum chamber as shown in **Figure 3**. The aim of the overall thermal management system is to maintain a battery module at an optimum average temperature, as dictated by life and performance trade-off. Important is that an even temperature, perhaps with small variations, is maintained between the cells and within the module. However, when designing such a system, regard must also be paid to the fact that the battery module should be compact, lightweight, have low cost manufacture and maintenance, and have easy access for maintenance. The management system should also have low parasitic power, allow the module to operate under a wide range of climatic conditions and provide ventilation if the battery generates potentially hazardous gases.

The calculation domain has two subdomains, that is, a fluid region and a solid region.

2.2.1. Fluid section

For non-steady flow, the equations of continuity, momentum and energy can be expressed in the general conservation form

$$\frac{\partial}{\partial t}(\rho\varphi) + \frac{\partial}{\partial x_i}(\rho u_i \varphi) = \frac{\partial}{\partial x_i}\left(\Gamma_\varphi \frac{\partial\varphi}{\partial x_i}\right) + S_\varphi \tag{20}$$

where ρ is the liquid density, u_i is the velocity vector components, Γ_φ is the effective exchange coefficient of φ and S_φ is the source rate per unit volume. The source rate and the effective exchange coefficient corresponding to each variable φ solved in this study are given in **Table 1**. Included in **Table 1** are the transport equations for the standard k-ε turbulence model.

In **Table 1**, μ is the viscosity, σ is the Prandtl number for ε and $G_k = \mu(\partial u_i/\partial x_j + \partial u_j/\partial x_i)$ $(\partial u_i/\partial x_j)$ the turbulence production rate. The values of the constants C_1 and C_2 are 1.44 and 1.92 respectively and for σ_k and σ_ε, 1.0 and 1.3 respectively [28]. The eddy viscosity term is

$$\mu_t = \rho C_\mu \frac{k^2}{\varepsilon} \tag{21}$$

where $C_\mu = 0.09$.

Equation	φ	S_φ	Γ_φ
Continuity	1	0	0
Momentum	U_i	$\frac{\partial p}{\partial x_i} + \rho_{ref}g_i$	$\rho(\mu + \mu_t)$
Enthalpy	h	$\frac{Dp}{Dt}$ + heat sources (sinks)	$\rho\left(\frac{\mu_t}{\sigma_t} + \frac{\mu}{Pr}\right)$
Kinetic energy of turbulence	k	$G_k - \rho\varepsilon$	$\frac{\mu}{\sigma_k}$
Eddy dissipation rate	ε	$C_1\left(\frac{\varepsilon}{k}\right)G - C_2\rho\left(\frac{\varepsilon^2}{k}\right)$	$\frac{\mu}{\sigma_\varepsilon}$

Table 1. Source rate and effective exchange coefficient for each φ.

In addition to the standard k-ε turbulence model, the realisable k-ε model with standard wall functions, and, non-equilibrium wall functions for the near-wall treatments were used to model turbulent flow as they show good performance in modelling flow structures [29, 30]. Although low-Reynolds number modelling (LRNM) may give more accurate simulation results, this requires very fine cells close to the wall to resolve the near wall region, which increases the difficulties of grid generation and computing time cost. Also the grid used by LRNM is unsuitable for the high-Reynolds number turbulence models used here because the very fine cells close to the wall cannot satisfy the first node near the wall located out of the viscous sub-layer [31]. The equations for the realisable k-ε turbulence model are

$$\frac{\partial}{\partial t}(\rho k) + \frac{\partial}{\partial x_j}(\rho k u_j) = \frac{\partial}{\partial x_j}\left(\left(\mu + \frac{\mu_t}{\sigma_k}\right)\frac{\partial k}{\partial x_j}\right) + G_k - \rho\varepsilon \tag{22}$$

$$\frac{\partial}{\partial t}(\rho\varepsilon) + \frac{\partial}{\partial x_j}(\rho\varepsilon u_j) = \frac{\partial}{\partial x_j}\left(\left(\mu + \frac{\mu_t}{\sigma_\varepsilon}\right)\frac{\partial\varepsilon}{\partial x_j}\right) + C_1\rho S_\varepsilon - C_2\rho\frac{\varepsilon^2}{k + \sqrt{\mu\varepsilon}} \tag{23}$$

$$\mu_t = \rho C_\mu \frac{k^2}{\varepsilon} = \frac{1}{4.04 + A_s k u^*/\varepsilon} \tag{24}$$

$$u^* = \sqrt{S_{ij}S_{ij}\tilde{\Omega}_{ij}\tilde{\Omega}_{ij}}, \quad \tilde{\Omega}_{ij} = \Omega_{ij} - 2\varepsilon_{ijk}\omega_k \tag{25}$$

$$A_s = \sqrt{6}\cos\varphi', \quad \varphi' = \frac{1}{3}\cos^{-1}\left(\sqrt{6}W\right), \quad W = \frac{S_{ij}S_{ik}S_{jk}}{\tilde{S}^3} \tag{26}$$

$$\tilde{S} = \sqrt{S_{ij}S_{ij}}, \quad C_1 = \max\left[0.43, \frac{\tilde{\mu}}{\tilde{\mu}+5}\right] \tag{27}$$

where $\sigma_k = 1.0$, $\sigma_\varepsilon = 1.2$ and $C_2 = 1.9$. The standard wall functions used here are based on the work of Launder and Spalding [32] and have been found to be suitable for a broad range of wall-boundary flows. The law-of-the-wall for mean velocity gives

$$U^* = \begin{cases} y^* & (y^* > 11.225 \\ \dfrac{1}{\kappa}\ln(Ey^*) & (y^* < 11.225 \end{cases} \tag{28}$$

where

$$U^* = \frac{U_p C_\mu k_p^{1/2}}{\tau_w/\rho} \tag{29}$$

is the dimensionless velocity, and

$$y^* = \frac{\rho C_\mu^{1/4} k_p^{1/2} y_p}{\mu} \tag{30}$$

is the dimensionless distance from the wall and κ is the von Karman constant (=0.4187), E is the empirical constant (=0.9793), U_p is the mean velocity of the fluid at the near-wall node P, k_p is

the turbulence kinetic energy at the near-wall node P, y_p is the distance from the point P to the wall, and μ is the dynamic viscosity of the fluid. The temperature wall functions include the contribution from the viscous heating, and for incompressible flow calculations, the law-of-the-wall for the temperature field has the following composite form

$$T^* = \frac{(T_w - T_p)\left(C_\mu^{1/4}k_p^{1/2}\right)}{(q_w/\rho C_p)} = \begin{cases} Pr\, y^* & (y^* < y_T^* \\ Pr_t\left[\dfrac{1}{\kappa}\ln(Ey^*) + P\right] & (y^* > y_T^* \end{cases} \tag{31}$$

where P is given by Jayatilleke [33]

$$P = 9.24\left(\frac{Pr}{Pr_t} - 1\right)\left(\frac{Pr}{Pr_t}\right)^{-1/4} \tag{32}$$

where y_T^* is the dimensionless thermal sublayer thickness, C_p is the specific heat of the fluid, q_w the wall heat flux, T_p is the temperature at the first near-wall node P, T_w is the temperature of the wall, Pr is the molecular Prandtl number ($= \mu C_p/a'$), a' is the coefficient of heat diffusion, and Pr_t is the turbulent Prandtl number (-0.85 at the wall).

The standard wall functions tend to become less reliable when the flow situations depart from the ideal conditions and are subjected to severe pressure gradients and strong non-equilibrium. The non-equilibrium wall functions are introduced and can potentially improve the results in the above mentioned situations [34]. The law-of-the wall for mean temperature remains the same as in the standard wall functions already described and the log-law for mean velocity sensitised to the pressure gradient is

$$\frac{\tilde{U}C_\mu^{1/4}k^{1/2}}{\tau_w/\rho} = \frac{1}{\kappa}\left(E\frac{\rho C_\mu^{1/4}k^{1/2}y}{\mu}\right) \tag{33}$$

where

$$\tilde{U} = U - \frac{1}{2}\frac{dp}{dx}\left[\frac{y_v}{\rho\kappa\sqrt{k}}\ln\left(\frac{y}{y_v}\right) + \frac{y - y_v}{\rho\kappa\sqrt{k}} + \frac{y_v^2}{\mu}\right] \tag{34}$$

and y_v is the physical viscous sublayer thickness, and computed from

$$y_v = \frac{\mu y_v^*}{\rho C_\mu^{1/4}k_p^{1/2}} \tag{35}$$

where $y_v^* = 11.225$.

In this study, the Boussinesq model was used to treat the variable water density in which the water density is taken as a constant in all terms of the solved equations, except for the buoyancy term in the momentum equation

$$(\rho - \rho_0)g = -\rho_0\beta(T - T_0)g \tag{36}$$

where ρ_0 is the reference density of the water flow (kg/m^3); T_0 is the reference temperature (K); and, Eq. (37) is obtained by the Boussinesq approximation $\rho = \rho_0(1 - \beta \Delta T)$ to replace the buoyancy terms. This approximation is acceptable so long as changes in actual density are small. Specifically, it is valid when $\beta(T - T_0) \ll 1$, and should not be used if the temperature difference in the domain is large.

2.2.2. Solid section

The solid section in this work consists of three components, namely, the aluminium block, the wall of the helix coil and the battery module. When the velocity is set to zero in Eq. (20), the equation governing pure conductive heat transfer by diffusion is obtained, that is,

$$\frac{\partial}{\partial t}(\rho\varphi) = \frac{\partial}{\partial x_i}\left(\Gamma_\varphi \frac{\partial \varphi}{\partial x_i}\right) + S_\varphi \tag{37}$$

Conjugate heat transfer was used between the solid domain and fluid domain.

2.3. Boundary conditions and settings

The cooling fluid is modelled using the material properties of water calculated using the inlet temperature. The settings and boundary conditions are set out in **Tables 2** and **3**.

2.4. Grid dependence and computer storage

The requirements set out in two recent guidelines referring to good CFD practice [35, 36] were followed in the present work. Non-uniform structured Cartesian grids were used throughout this work with extensive tests for independence of grid size checked by increasing the grid numbers until further refinement was shown not to be of significance. Close to solid surfaces, the grid was refined using geometric progression with an expansion ratio from the solid surfaces of less than 1.1 and with the Y$^+$ values adjacent to a solid boundary held around a

Battery module outside dimensions	Radius = 130 mm, height = 360 mm
Cooling pipe radius (r_{inner})	5–15 mm
Coolant	H$_2$O
Final mesh size	10^7

Table 2. Various settings used during the calculations.

Cylinder outer wall	293.15 K
Coolant/solid interface	Conjugate heat transfer
Cooling pipe inlet	$u_{in} = 0.005 - 0.1$ m/s
Cooling pipe outlet	$T_{in} = 293.15$ K
Cell initial temperatures	101,325 Pa
	$T_{init} = 313.15$ K
	$T_{init} = 349.15$ K

Table 3. Boundary conditions used during the calculations.

value of 20, so complying with recommendations given in the literature that Y^+ should be between 11.5 and 300 to ensure accuracy when using a high-Reynolds turbulence model [37]. Tests for grid independent solutions were carried out using 2.0×10^5, 2.0×10^6 and 1.0×10^7. The overall change in the residual for each variable between the last two numbers of elements was less than 0.1%, indicating grid independence had been achieved. The calculations were performed on a Dell T5500 workstation with 32 nm six-core Intel Xeon 5600 series processor and main memory of 24 GB. A typical CPU time for a transient run with a grid having 10^6 nodes was just over 24 h.

3. Results

3.1. Heat generation within a single cell

The thermal characteristics of a Li-ion battery cell are first investigated using Eqs. (1)–(19), which form thermal-electrochemical coupled model. The cell used in these calculations has an electrolyte consisting of zinc and lithium salts dissolved in water. When the battery is fully charged, the anode consists of nonporous zinc and the cathode of porous Mn_2O_4. It is important to note that some of the electrochemical calculations are strongly dependent on coefficients, which are in turn strongly dependent of experimental results. For example, for the electrolyte just described, the specific conductivity Eq. (11) of the electrolyte is a function of temperature and the concentration of the electrolyte in the liquid phase, and so the ionic conductivity, κ_i had to be determined by experiment, the results of which are summarised in **Figure 4**.
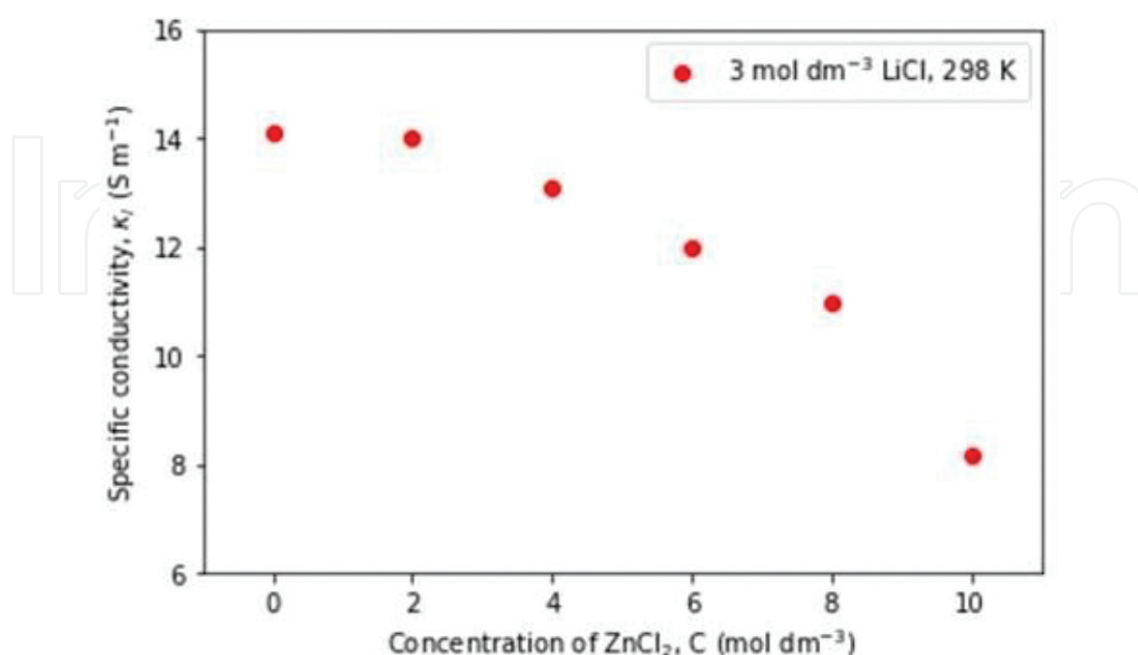

Figure 4. Ionic conductivity of electrolyte consisting of a $ZnCl_2$ and LiCl aqueous solution.

The effect of using different current rates during discharge of the battery cell is illustrated in **Figure 5**. Here temperature on the cell surface is calculated against the depth of discharge (DOD), which indicates the state of discharge of the battery cell starting at 100% fully charged. In these calculations, DOD was calculated as time $* \frac{C \text{ rate}}{3600}$ and the heat transfer coefficient h was set at $1.0 \, \text{Wm}^{-2} \, \text{K}^{-1}$. As would be expected, the cell surface gets hotter as the discharge current rate increases. There is a 'kink' in the curve at lower current rates, which is thought to be due to an interaction between the ohmic and reversible heat in the energy balance equation.

Also calculated were the profiles of cell surface temperatures over a long time of discharge. Two limiting cases, that is, adiabatic and isothermal were used as the boundaries for this study with different heat transfer coefficients used for the intervening calculations, as shown in **Figure 6**. It can be seen that the heat transfer coefficient $1.0 \, \text{W}^{-2} \, \text{K}^{-1}$ gives a reasonable result and keeps the battery cell well within the desired operating range, while the $0.1 \, \text{W}^{-2} \, \text{K}^{-1}$ setting allows the battery cell wall temperature to reach the upper region of the desired range.

3.2. Cooling the battery module

In this part of the study, the temperature history of the battery module was modelled with ambient conditions (T_∞) set at 293.15 K, and each of the cells sets initially at T_{init}=313.15 K and then at T_{init}=349.15 K. This part of the calculations is important to the design process in that, in addition to testing, if the chosen geometry parameters are suitable, it also gives an indication concerning the selection of a suitable pump and heater/refrigeration unit. Typical velocity contours for the liquid coolant are shown in **Figure 7**. The important part here is that heat can be removed from the coolant in the plenum chamber efficiently. From **Figure 7**, it can be seen that there is slow moving water adjacent to the heating/refrigeration unit, and hence there is sufficient time for dissipation of heat.
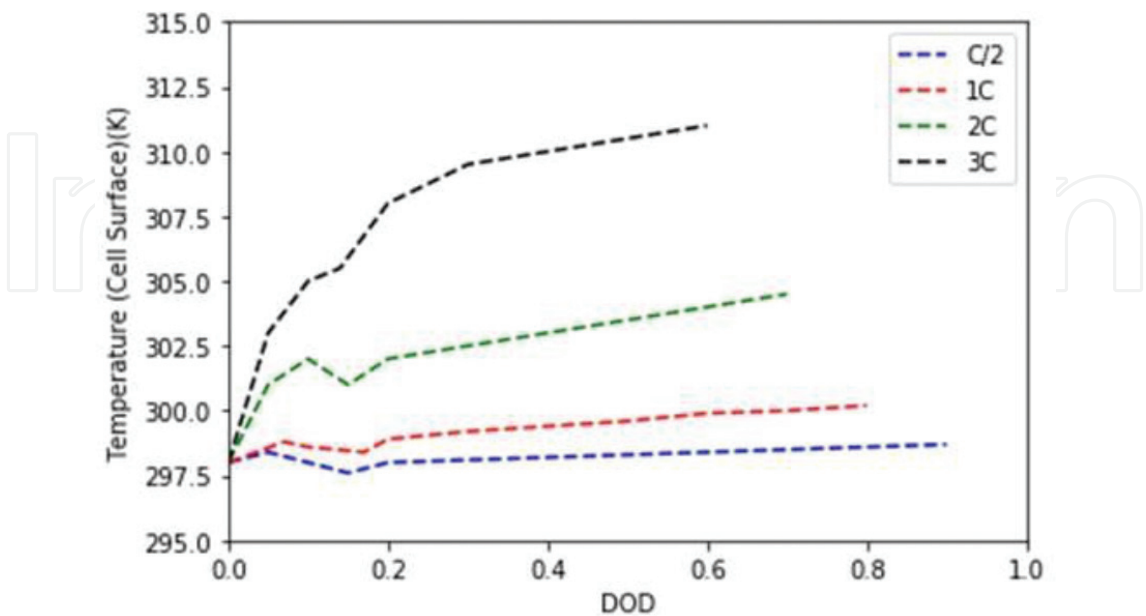

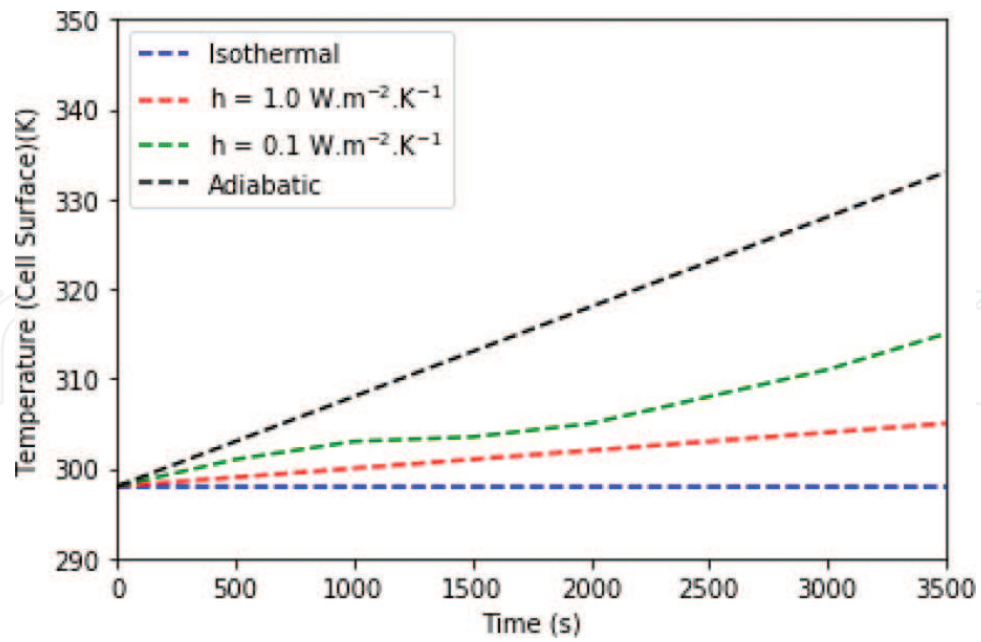**Figure 5.** Cell surface temperature during discharge at different current rates.

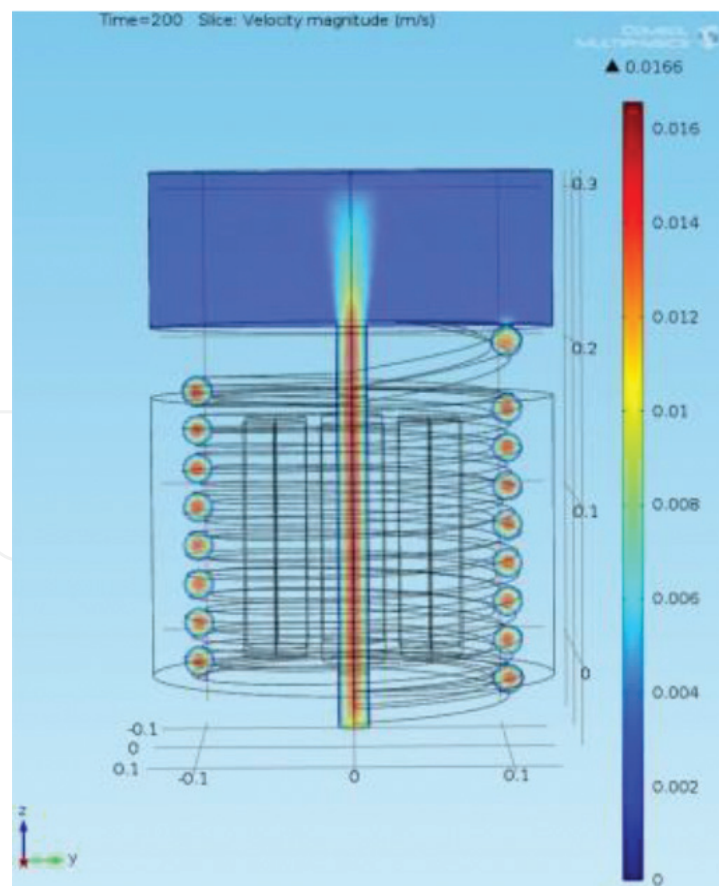**Figure 6.** Cell surface temperature for different cooling conditions.

Figure 7. Velocity contours, $u_{in} = 0.01$ m/s, $T_{in} = 293.15$ K, $r_{inner} = 10$ mm, $T_{\infty} = 293.15$ K.

Several tests were conducted, where the battery module was cooled to find appropriate values for the parameters, u_{in} and the optimum number of helix coil turns. **Figure 8** shows temperature values obtained at the centre of a cell versus time during cooling. The figure shows results for two initial cell temperatures, that is, 313.15 and 349.15 K, and the temperature profiles were obtained for different inlet velocities to the helix tube ranging from 0.005 to 0.1 m/s. It was found that when using an inlet velocity of 0.005 m/s, the cell temperature did not reach an acceptable temperature over what was regarded as a reasonable time. When the inlet velocity was increased to 0.01 m/s, acceptable temperatures were calculated after 80 and 20 s for the higher and lower initial temperatures, respectively. With the much higher inlet velocity of coolant to the helix pipe, that is, 0.1 m/s, there was a definite faster reduction in temperature. However, this faster velocity has design implications in that more powerful pumps together with a greater danger of coolant leakage make use of this inlet velocity value less attractive. Therefore, it was decided to continue the study with $u_{in} = 0.01$ m/s. It is also noticeable from **Figure 8** that as the initial temperature of the cells was reduced, increasing the velocity of the coolant through the pipe had much less effect on the cooling rate. This could mean that, although the coolant at higher velocity had more capacity to carry heat energy away from the battery pack, the temperature gradient between solid helix pipe and water was no longer sufficient to drive heat energy from solid to liquid effectively. This could possibly be due to the complex nature of the flow within the helix tube. Inside the tube, the flow is stretched from the inner wall, where most of the heat energy enters the liquid towards the outer wall due to centrifugal forces. Secondary flow also results due to the centrifugal forces. This aspect of the design needs further research.

It is important to know the optimum number of turns the helix coil makes for a number of reasons. One is that if too many coils are used, then more expense occurs in the manufacturing
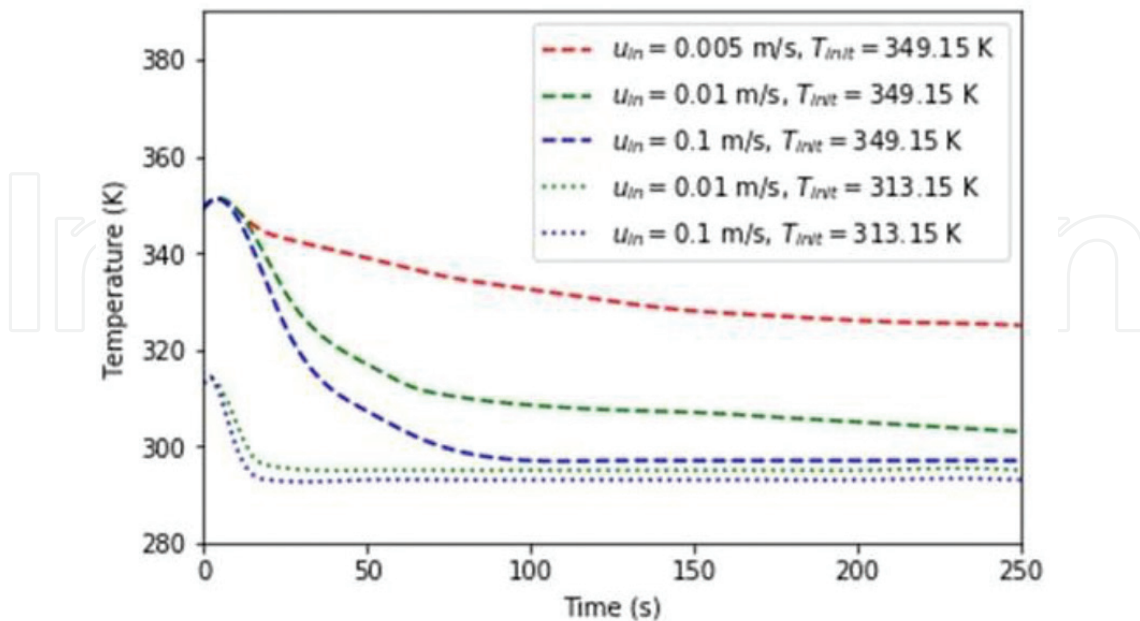

Figure 8. Temperature cooling profiles versus time at the centre of a cell for different initial cell temperatures and fluid velocities in the helix tube. Here $r_{inner} = 10$ mm, $T_\infty = 293.15$ K and $T_{in} = 293.15$ K.

stage and also the integrity of the structure may suffer. If the number of coils is too small, then cooling of the battery to its ideal operating temperature range may become unacceptable. As can be seen from **Figure 9**, there is a big advantage to the cooling system when increasing the number of turns for 5 to say 15, but after that, the cooling effect of increasing the number of turns is greatly diminished. Increasing the number of turns is equal to lengthening the heat transfer path. According to **Figure 9**, as the number of turns increases, the amount of the heat transfer coefficient decreases significantly and after, say, 15 turns, it remains almost constant. The Prandtl number for water is larger than the one which would make the thermal entrance greater than the hydraulic entrance length. This means that after about 15 turns the thermal entrance length has been passed. An optimum number of turns appear to be around 10. The rest of this study continues with the number of helix turns in the aluminium block to be 10.

It is important for the lengthening of battery cell life and the enhancement of charging and discharging performance that uniformity of temperature is achieved throughout each cell, in addition to uniformity of cell temperatures across the cells within the battery module. To confirm that uniformity of temperature could be achieved across a single cell lodged within the battery module, temperature profiles were calculated in the radial direction through the battery module. As can be seen from **Figure 10**, where the radius at 0 is the battery module centre and radius at 130 mm is the outer wall of the module, the temperature profiles gradually move from an initial profile distorted by the hot cell to an acceptable final uniform distribution after about 15 s.

Another series of tests were conducted on the battery module which had, in addition to initial temperatures of 313.15 and 349.15 K, an internal heat source for each cell of either 0.25, 0.5 or 1 W. Results for the module with each of the cells having internal heat sources of 1 W are
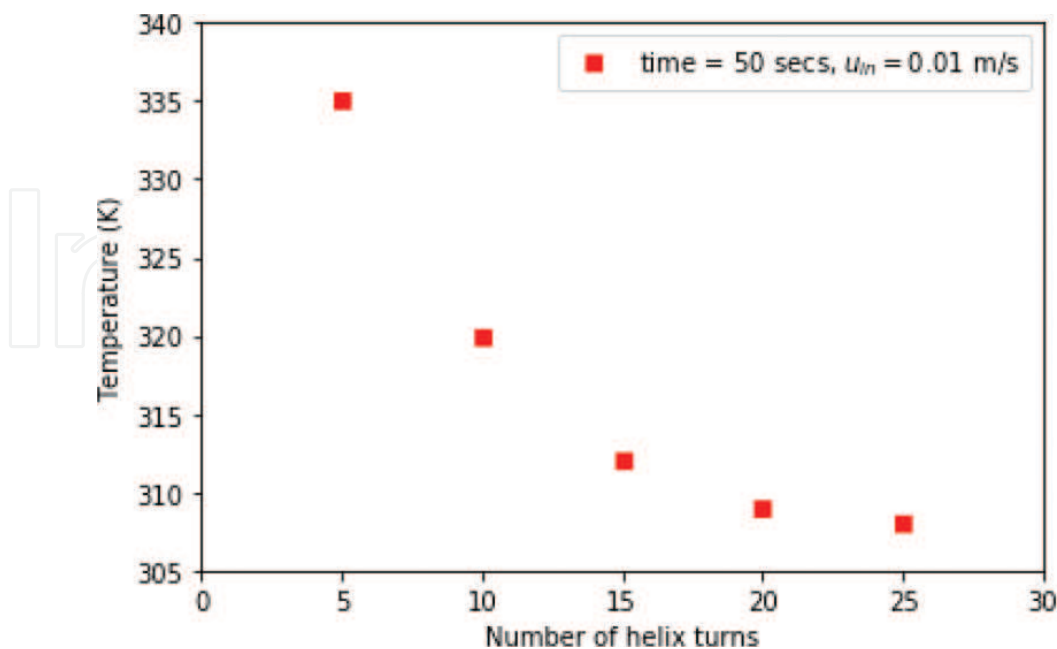

Figure 9. Temperature values at the centre of a cell for different number of helix coil turn after 50 s. Here, $T_{init} = 313.15$ K, $u_{in} = 0.01$ m/s, $r_{inner} = 10$ mm, $T_\infty = 293.15$ K, $T_{in} = 293.15$ K.

shown in **Figures 11** and **12**. As with the previous tests, what was important was the control of temperature between acceptable limits and a good uniformity of temperature across each cell.

It can be seen from **Figures 11** and **12** that in the early stages of cooling, non-uniformity was found, but after, say, 1 min, uniformity was acceptable throughout each cell, and after 2 min, each cell was within the desired operating temperature limits (Note: each sub-figure has its
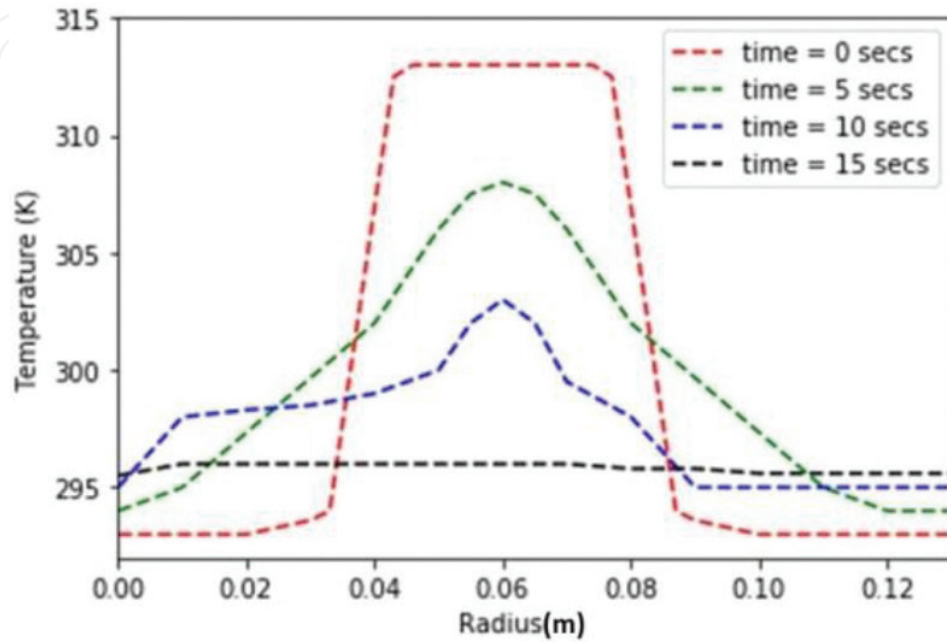

Figure 10. Temperature profiles in the radial direction for $T_{init} = 313.15$ K, $u_{in} = 0.01$ m/s, $r_{inner} = 10$ mm, $T_\infty = 293.15$ K, $T_{in} = 293.15$ K.
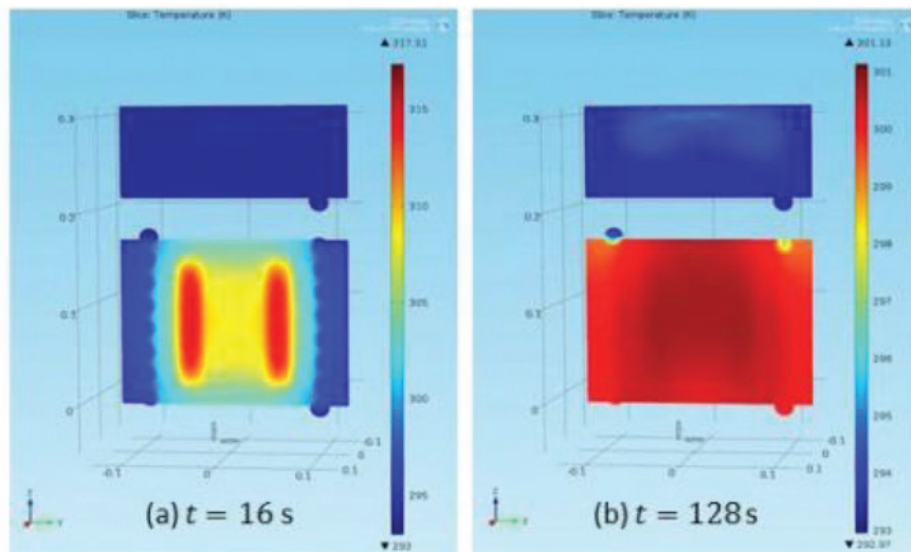

Figure 11. Front view of temperature profiles for $T_{init} = 313.15$ K, $u_{in} = 0.01$ m/s, $r_{inner} = 10$ mm, $T_{in} = 293.15$ K, and heat source within each cell of 1 W.
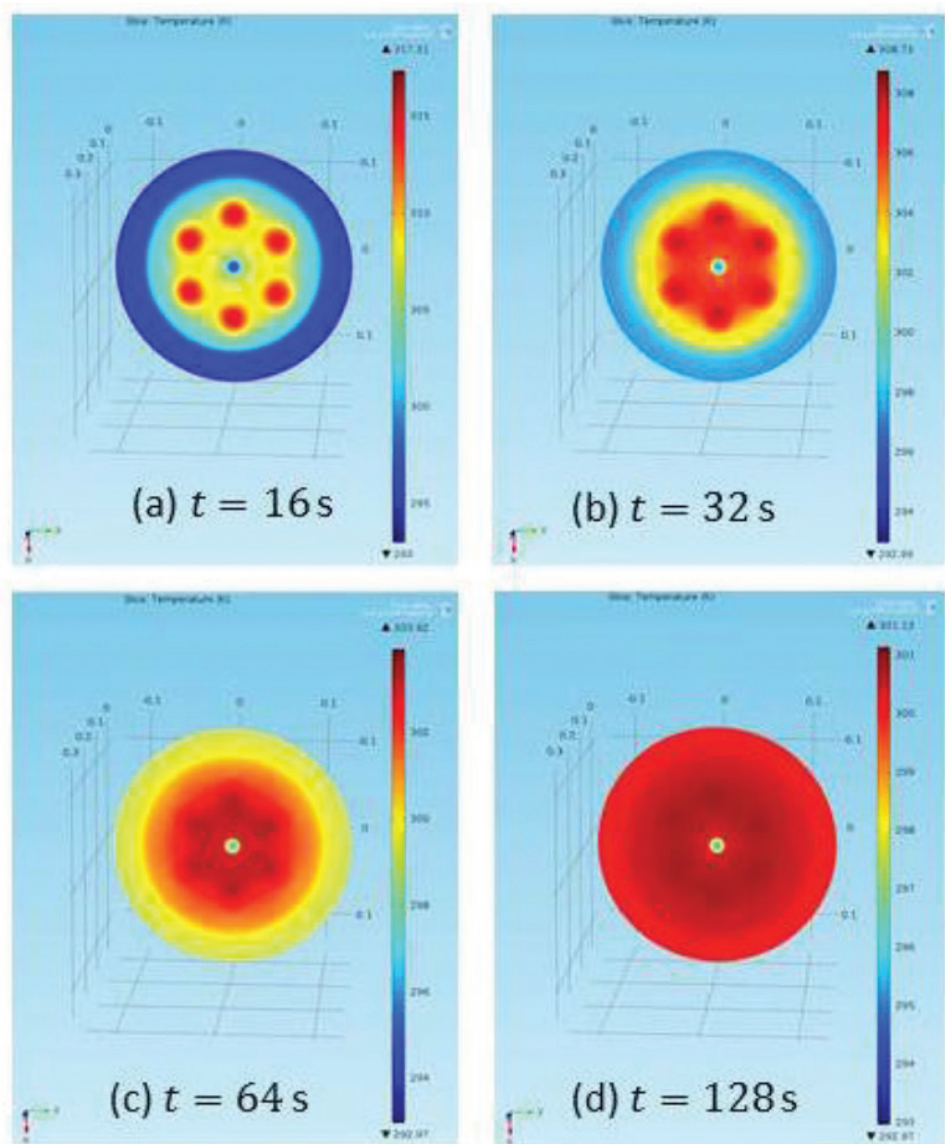
Figure 12. Plan view of temperature profiles for T_{init} =313.15 K, $u_{in} = 0.01\,\mathrm{m/s}$, $r_{inner} = 10$ mm, $T_{in} = 293.15$ K, and heat source within each cell of 1 W.

own temperature scale). At times greater than 2 min, the heat loss to the atmosphere was slightly higher than heat production within the cells, even at 1 W, so reducing the need for further cooling. In the propose prototype, the temperature would be monitored using a thermostat, and further cooling would ensue intermittently as necessary.

4. Conclusion(s)

Preliminary results useful to the final design of a prototype battery module have been produced. The values found for the important parameters help in confirming the chosen geometry, and give indications of necessary pump and heating/refrigeration specifications needed when assembling

the prototype. The calculations were made first inside a given battery cell to indicate what sort of temperature differences may be expected. It was found that these calculations depended heavily on experimental work to find appropriate coefficients for the coupled equations. After getting the range of temperatures arising from single battery cell calculations, a method was developed to find the temperature characteristics of the battery module, with stress being put on uniformity of temperature both within an individual cell and across the complete battery module.

Conflict of interest

There is no conflict of interest associated with this chapter.

Nomenclature

a	specific surface area, m^{-2}
c	electrolyte concentration in the solution phase, mol^{-3}
c_s	Li concentration in electrode particles, $mol\ m^{-3}$
C_1, C_2	k-ε turbulence model constants
C_p	specific heat
C_μ	turbulence model coefficient
D_{eff}	effective diffusion coefficient of Li in the electrode
D_s	diffusion coefficient of Li in electrode particles, $m^2\ s^{-1}$
E	potential
F	Faraday's constant
h	heat transfer coefficient
I	current
J	surface reaction flux, $mol\ m^{-2}\ s^{-1}$
J_i	pore wall flux
k	turbulence kinetic energy
k_p	turbulence kinetic energy at near wall node
k_T	lumped thermal conductivity of cell
L_n	anode thickness, m
L_p	cathode thickness, m

L_s separator thickness

Pr   Prandtl number

q_w wall heat flux

$\dot{Q}_{rea}$ heat generation due to electrochemical reaction

$\dot{Q}_{rev}$ reversible heat

$\dot{Q}_{ohm}$ ohmic heat

r radius/radial

R universal gas constant

t time

t_+^0 transference number

T temperature

T_∞ ambient temperature

T_0 reference temperature

T_w wall temperature

U mean velocity

U_i open circuit voltage

x_i spatial coordinates

y_v viscous sublayer thickness

y^+ dimensionless velocity

Greek letters

β constant, Boussinesq model

ε dissipation

ε' volume fraction of electrolyte

η_i overpotential

κ von Karman constant

λ coefficient, Newton's cooling law

μ absolute viscosity

ρ density

ρ_0　　reference density

σ_{eff}　　effective electric conductivity

σ_k　　constant in turbulence model

σ_ε　　constant in turbulence model

τ_w　　wall shear stress

ϕ　　potential

Γ_φ　　effective exchange coefficient

Author details

Desmond Adair*, Kairat Ismailov and Zhumabay Bakenov

*Address all correspondence to: dadair@nu.edu.kz

Nazarbayev University, Astana, Kazakhstan

References

[1] Aifantis KE, Hackney SA, Kumar RV. High Energy Density Lithium Batteries: Materials, Engineering, Applications. New York: Wiley; 2010

[2] Ramadass P, Haran B, White R, Popov BN. Capacity fade of Sony 18650 cells cycled at elevated temperatures: Part I. Cycling performance. Journal of Power Sources. 2002; **112**(2):606-613

[3] Ramadass P, Haran B, White R, Popov BN. Capacity fade of Sony 18650 cells cycled at elevated temperatures: Part II. Capacity fade analysis. Journal of Power Sources. 2002; **112**(2):614-620

[4] Pinson MB, Bazant MZ. Theory of SEI formation in rechargeable batteries: Capacity fade, accelerated aging and lifetime prediction. Journal of the Electrochemical Society. 2013;**160**: A243-A250

[5] Zhang SS, Xu K, Jow TR. The low temperature performance of Li-ion batteries. Journal of Power Sources. 2003;**115**(1):137-140

[6] Fan J. On the discharge capability and its limiting factors of commercial 18650 Li-ion cell at low temperatures. Journal of Power Sources. 2003;**117**:170-178

[7] Wang Q, Ping P, Zhao X, Chu G, Sun J, Chen C. Thermal runaway caused fire and explosion of lithium ion battery. Journal of Power Sources. 2012;**208**:210-224

[8] Fan L, Khodadadi JM, Pesaraan AA. Parametric study on thermal management of an air-cooled lithium battery module for plug-in hybrid electric vehicles. Journal of Power Sources. 2013;**247**(3):961-966

[9] Ling Z, Wang F, Fang X, Gao X, Zhang Z. A hybrid thermal management system for lithium ion batteries combining phase change materials with forced-air cooling. Applied Energy. 2015;**148**:403-409

[10] Mahamud R, Park C. Reciprocating air flow for Li-ion battery thermal management to improve temperature uniformity. Journal of Power Sources. 2011;**196**(13):5685-5696

[11] Yang N, Zhang X, Li G, Hua D. Assessment of the forced air-cooling performance for cylindrical lithium-ion battery packs: A comparative analysis between aligned and staggered cell arrangements. Applied Thermal Engineering. 2015;**80**:55-65

[12] Amiribavandpour P, Shen W, Mu D, Kapoor A. An improved theoretical electrochemical-thermal modelling of lithium-ion battery packs in electric vehicles. Journal of Power Sources. 2015;**284**:328-338

[13] Ye Y, Shi Y, Cai N, Lee J, He X. Electro-thermal modeling and experimental validation for lithium-ion battery. Journal of Power Sources. 2012;**199**:227-238

[14] Cai L, White RE. Mathematical modelling of lithium ion battery with thermal effects in COMSOL Inc multiphysics software. Journal of Power Sources. 2011;**196**:5985-5989

[15] Gu WB, Wang CY. Thermal-electrochemical modeling of battery systems. Journal of the Electrochemical Society. 2000;**147**(8):2910-2922

[16] Anwar S, Zou C, Manzie C. Distributed thermal-electrochemical modeling of a lithium-ion battery to study the effect of high charging rates. The International Federation of Automatic Control; 24-29 August, 2014; Cape Town, South Africa

[17] Sabbah R, Kizilel R, Selman JR, Al-Hallaj S. Active (air-cooled) vs. passive (phase change material) thermal management of high power lithium-ion packs: Limitation of temperature rise and uniformity of temperature distribution. Journal of Power Sources. 2008; **182**(2):630-638

[18] Pesaran AA, Burch S, Keyser M. An approach for designing thermal management systems for electric and hybrid vehicle battery packs. Fourth Thermal Management Systems Conference and Exhibition; 24-27 May, 1999; London, UK

[19] Klien R, Chaturvedi NA, Christensen J, Ahmed J, Findeisen R, Kojic A. Electrochemical model based observer design for a lithium-ion battery. IEEE Transactions on Control Systems Technology. 2013;**21**(2):289-301

[20] Karimi G, Li X. Thermal management of lithium-ion batteries for electric vehicles. International Journal of Energy Research. 2013;**37**:13-24

[21] Ismailov K, Adair D, Massalin Y, Bakenov Z. On using splitter plates and flow guide-vanes for battery module cooling. Heat and Mass Transfer. 2017;**53**(1):1-10

[22] Chen K, Li X. Accurate determination of battery discharge characteristics - a comparison between two battery temperature control methods. Journal of Power Sources. 2014;**247**(3): 961-966

[23] Yeow K, Teng H, Thelliez M, Tan E. Thermal analysis of a Li-ion battery systems with indirect liquid cooling using finite element analysis approach. SAE International Journal of Alternative Power. 2012;**1**(1):65-78

[24] Tong W, Somasundaram K, Birgersson E, Mijumdar AS, Yap C. Numerical investigation of water cooling for a lithium-ion bipolar battery pack. International Journal of Thermal Science. 2015;**94**:259-269

[25] Pesaran AA. Battery thermal management in EVs and HEVs: Issues and solutions. Advanced Automotive Battery Conference; 6-8 Feb., 2001; Las Vegas, Nevada

[26] Doyle M, Fuller TF, Newman J. Modeling of galvanostatic charge and discharge of the lithium/polymer/insertion cell. Journal of the Electrochemical Society. 1993;**140**:1526-1533

[27] Valoen LO, Reimers N. Transport properties of LiPF6 - based li-ion battery electrolytes. JES. 2005;**152**:A882-A891

[28] Adair D. Numerical calculations of aerial dispersion from elevated sources. Applied Mathematical Modelling. 1990;**14**:459-467

[29] Allegrini J, Dorer V, Carmeliet J. Buoyant flows in street canyons: Validation of CFD simulations with wind tunnel measurements. Building and Environment. 2014;**72**:63-74

[30] van Hooff T, Blocken B. Coupled urban wind flow and indoor natural ventilation modelling on a high-resolution grid: A case study for the Amsterdam arena stadium. Environment Modelling and Software. 2010;**25**(1):51-65

[31] Tao WQ. Numerical Heat Transfer. 2nd ed. Xi'an: Xi'an Jiaotong University Press; 2001

[32] Launder BE, Spalding DB. The numerical computational of turbulent flows. Computer Methods in Applied Mechanics and Engineering. 1974;**3**(2):269-289

[33] Jayatillaka C. The influence of Prandtl number and surface roughness on the resistance of the laminar sublayer to momentum and heat transfer. Progress in Heat and Mass Transfer. 1969;**1**:193-321

[34] Kim SE, Choudhury D. A near-wall treatment using wall functions sensitized to pressure gradient. In F.E.D. ASME, editors, Symp. on Separated and Complex Flows. 1995;**217**:249-256

[35] Tominaga Y, Mochida A, Yoshie R, Kataoka H, Nozu T, et al. All guidelines for practical applications of CFD to pedestrian wind environment around buildings. Journal of Wind Engineering and Industrial Aerodynamics. 2008;**96**:1749-1761

[36] Meroney R, Ohba R, Leitl B, Kondo H, Grawe D, Tominaga Y. Review of CFD guidelines for dispersion modeling. Fluids. 2016;**1**(14):1-16

[37] Patankar SV. Numerical Heat Transfer and Fluid Flow. New York: CRC Press; 1980